Photoacoustics 26 (2022) 100355

Contents lists available at ScienceDirect

Photoacoustics

journal homepage: www.elsevier.com/locate/pacs

# Multi-modal imaging for uptake of peptide ligand specific for CD44 by hepatocellular carcinoma

Xiaoli Wu [a,1], Xiaoqing Meng [a,1], Tse-Shao Chang [b], Shuo Feng [a], Miki Lee [a], Sangeeta Jaiswal [a], Eun-Young K. Choi [c], Lam Tran [d], Hui Jiang [d], Thomas D. Wang [a,b,e,*]

[a] Department of Internal Medicine, Division of Gastroenterology, University of Michigan, Ann Arbor, MI 48109, USA
[b] Department of Mechanical Engineering, University of Michigan, Ann Arbor, MI 48109, USA
[c] Department of Pathology, University of Michigan, Ann Arbor, MI 48109, USA
[d] Department of Biostatistics, University of Michigan, Ann Arbor, MI 48109, USA
[e] Department of Biomedical Engineering, University of Michigan, Ann Arbor, MI 48109, USA

ARTICLE INFO

*Keywords:*
CD44
Peptide
Hepatocellular carcinoma
Liver
Cancer
Fluorescence
Photoacoustic

ABSTRACT

*Background:* Hepatocellular carcinoma (HCC) is rising steadily in incidence, and more effective methods are needed for early cancer detection and image-guided surgery.
*Methods:* We used a structural model to optimize the peptide sequence. Specific binding was validated in vitro with knockdown, competition, and co-localization assays. Multi-modal imaging was performed to validate specific binding in vivo in orthotopically-implanted human xenograft tumors.
*Results:* Binding properties of WKGWSYLWTQQA were characterized by an apparent dissociation constant of $k_d$ = 43 nM, and an apparent association time constant of k = 0.26 $min^{-1}$. The target-to-background ratio was significantly higher for the target versus control for both modalities. Ex-vivo evaluation using human HCC specimens supported the ability of the peptide to distinguish HCC from other liver pathologies.
*Conclusions:* We have identified a peptide specific for CD44 with properties that are promising for clinical translation to image HCC in vivo.

## 1. Introduction

Hepatocellular carcinoma (HCC) accounts for over 840,000 deaths globally, and is emerging rapidly as a major contributor to the worldwide healthcare burden [1–4]. Because few patients are diagnosed early, the 5-year survival rate is < 7%, and the median survival length is < 1 year [5]. In the U.S., the incidence of HCC is rising steadily, and is currently growing faster than that of any other cancer [6]. Conventional methods for liver imaging excel at providing anatomical features of masses. Ultrasound is recommended for patients with cirrhosis, but in general cannot distinguish between malignant and benign lesions [7]. Contrast-enhanced CT and MRI detect HCC based on increased vascularity, but cannot clarify pathology for liver nodules < 1–2 cm in diameter [8]. Malignant hepatocytes uniquely overexpress targets that can be developed for improved HCC diagnosis and therapy [9]. Thus, early detection of HCC remains a major healthcare challenge globally, and novel diagnostic options are urgently needed [10,11].

CD44 (cluster of differentiation 44) is an emerging tissue biomarker for HCC [12–14]. The standard isoform is denoted as CD44s, which regulates TGF-β signaling [15], and spliced variants are denoted as CD44v. Positive staining for CD44s was found on the hepatocyte membrane in up to 84% of early-stage HCC specimens using immunohistochemistry [16–18]. A smaller percentage was positively identified for CD44 variants [19–21]. CD44 is a transmembrane glycoprotein that binds to hyaluronic acid, a component of the extra-cellular matrix and a mediator of fibrogenesis that leads to cirrhosis [22]. CD44 serves an adhesion molecule, enables communication by cell-cell signal transduction, and regulates a number of biological processes within liver cells

*Abbreviations:* CD44, cluster of differentiation 44; HCC, hepatocellular carcinoma; H&E, hematoxylin & eosin; ICG, indocyanine green; IHC, immunohistochemistry; NIR, near infrared; T/B, target-to-background.

* Correspondence to: Biomedical Engineering, and Mechanical Engineering Division of Gastroenterology, University of Michigan, 109 Zina Pitcher Pl. BSRB 1522, Ann Arbor, MI 48109-2200, USA.
*E-mail address:* thomaswa@umich.edu (T.D. Wang).

[1] Authors contributed equally

https://doi.org/10.1016/j.pacs.2022.100355
Received 23 November 2021; Received in revised form 25 March 2022; Accepted 8 April 2022
Available online 11 April 2022

[23]. CD44 has various functions in cell division, migration, adhesion, and signaling, and enables cells to interact either through the intracellular matrix or through cellular junctions. CD44 has recently been demonstrated to be a universal marker for cancer stem cells/tumor initiating cells (CSCs/TICs) [24–28].

Peptides that bind specifically to cell surface targets can be developed with high affinity and fast kinetics [29–31]. Peptides can diffuse and extravasate through leaky vessels to achieve high concentrations and deep penetration in solid tumors. Tumor uptake in vivo can occur within a few hours [32]. This time scale is compatible with clinical use for early detection and image-guided surgery. Peptides clear quickly from the circulation to avoid toxicity to viable liver, and minimize biodistribution to non-target tissues. Peptide-based ligands have properties that are well matched for in vivo delivery to tumors that arise from cirrhotic livers. Their small size and low molecular weight facilitate challenging navigation obstacles, including irregular microvasculature, heterogeneous uptake, and transport barriers [33–35]. Also, peptides have low potential for immunogenicity [36,37]. Here, we aim to identify and validate a peptide specific for CD44, and demonstrate feasibility for future clinical translation.

## 2. Results

### 2.1. Peptide specific for CD44

Alignment between candidate peptide sequences and the CD44 target was evaluated using CABS-dock software [38,39]. The crystal structure (1UUH) for the extracellular hyaluronan binding domain of CD44s was obtained from the Protein Data Bank (PDB) [40]. A library of candidate peptide sequences was generated and assessed individually using a contact map, Fig. S1. Pairs of peptide/target residues $< 4.5$ Å in proximity were identified, Table S1. Amino acids that paired more than 5 times with the target were chosen, Fig. S2 (red box). The docking energy for candidate peptides binding to 1UUH was determined using Hex 8.0.0 protein-ligand docking software [41]. The sequence WKGWSYLWTQQA, hereafter WKG*, was found to bind CD44 with a total energy $E_t = -534$, Fig. S3A. This sequence was scrambled as WYKAQQWWTLGS, hereafter WYK*, for use as control and resulted in $E_t = -494$, Fig. S3B.

### 2.2. Peptide synthesis

The C-terminus of this peptide was covalently linked with IRDye800, a near-infrared (NIR) fluorophore, via a GGGSC linker, hereafter WKG* -IRDye800, Fig. 1A. The linker separates the peptide from the fluorophore and prevents steric hindrance. The scrambled sequence was also labeled with IRDye800, hereafter WYK* -IRDye800, Fig. 1B. 3D models are shown to highlight differences between the biochemical structures, Fig. 1C,D. The peptides were synthesized with $>$ 95% purity by HPLC, and an experimental mass-to-charge ratio ($m/z$) of 1913.87 was measured using mass spectrometry, which agrees with expected value of 1913.88, Fig. S4A,B.

### 2.3. Spectral measurements

Peak absorbance and emission occur in the near-infrared (NIR) spectrum where hemoglobin absorption, tissue scattering, and tissue autofluorescence are minimal, Fig. S5A,B.

### 2.4. siRNA knockdown

CD44 expression was knocked down in human SK-Hep1 HCC cells using siRNA to validate specific binding of WKG* -IRDye800 to CD44. WKG* -IRDye800 and anti-CD44-AF488 antibody showed strong binding to the surface (arrows) of SK-Hep1 cells transfected with siCL (control) using confocal microscopy, while WYK* -IRDye800 displayed minimal binding, Fig. 2A. Fluorescence intensities from SK-Hep1 cells with knockdown of CD44 showed minimal intensity with either peptide, Fig. 2B-D. Quantified results showed this decrease to be significant, Fig. 2E. Western blot confirms effective knockdown of CD44 in SK-Hep1 cells, Fig. 2F. Binding by WKG* -IRDye800 and anti-CD44-AF488 to the surface (arrows) of Sk-Hep1 cells co-localizes with a correlation of

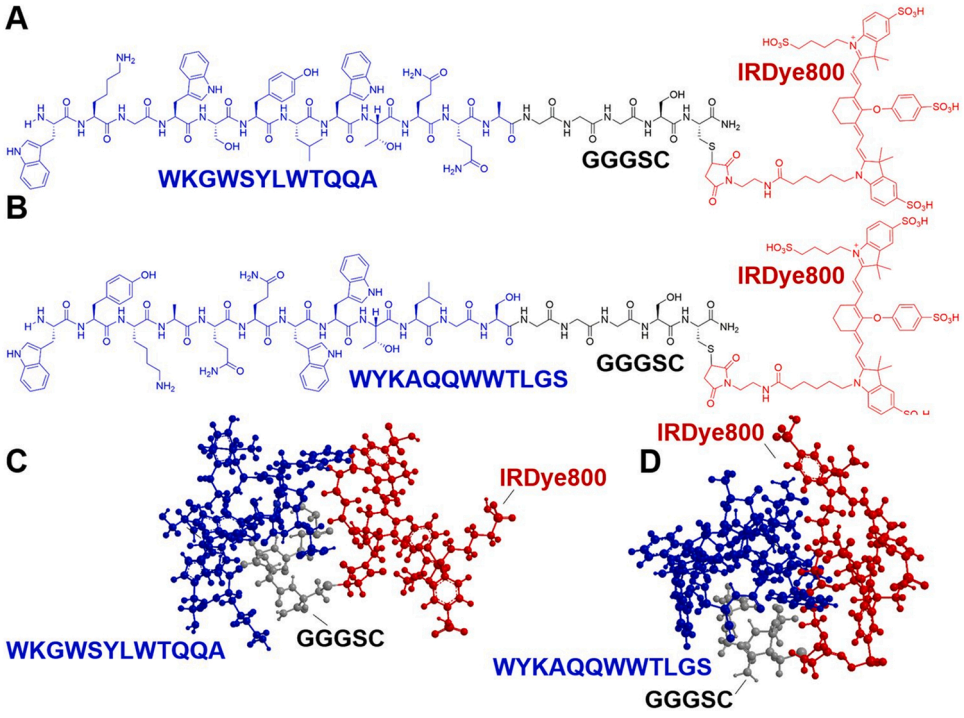


**Fig. 1.** Optimized peptide sequence specific for CD44. (A) WKGWSYLWTQQA (blue) is labeled with IRDye800 (red) via a GGGSC linker (black). (B) The sequence is scrambled as WYKAQQWWTLGS for use as control. (C,D) 3D models show differences in biochemical structures.

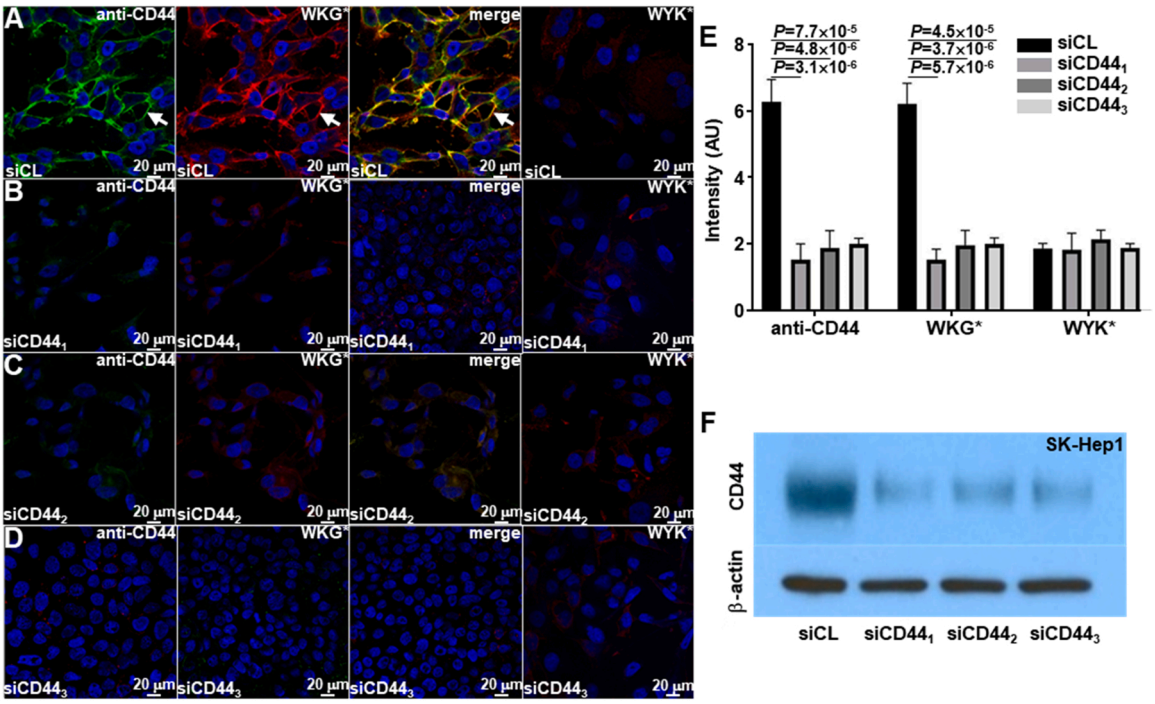


**Fig. 2.** Validation of specific peptide binding with siRNA knockdown. (A) Anti-CD44-AF488 (green) and WKG* -IRDye800 (red) show strong binding to the surface (arrows) of human SK-Hep1 HCC cells transfected with control siRNA (siCL). Co-localization of binding can be appreciated on the merged image. The scrambled control WYK* -IRDye800 shows minimal binding. (B-D) The fluorescence intensities measured for anti-CD44-AF488 and WKG* -IRDye800 are greatly reduced with knockdown of CD44 using 3 different siRNAs. WYK* -IRDye800 shows little binding to knockdown cells. (E) Quantification of fluorescence intensities show a significant difference in intensities for anti-CD44-AF488 (siCL 4.1, 3.3, and 3.1-fold change in intensity relative to siCD441, siCD442, siCD443) and WKG* IRDye800 (4.0, 3.1, 3.1-fold change). WYK* IRDye800 shows no significant differences. (F) Western blot shows CD44 expression for control (siCL) and knockdown (siCD44) cells.

$\rho = 0.81$ measured on the merged image, Fig. S6.

### 2.5. Confocal fluorescence microscopy

Significantly greater fluorescence intensity was observed for binding of WKG* -IRDye800 and anti-CD44-AF488 to SK-Hep1 cells (CD44 +) compared with Hep 3B cells (CD44-) cells, Fig. S7.

### 2.6. Peptide characterization

Specific binding of WKG* -IRDye800 to CD44 was further supported by addition of unlabeled WKG* to compete for binding. Fluorescence intensities from SK-Hep1 cells decreased significantly with increasing concentrations of unlabeled WKG* , Fig. 3A, but not with WYK* , Fig. 3B. Quantified results show the decrease to be concentration dependent, Fig. 3C. These results suggest that the peptide rather than either the linker or fluorophore mediates the binding interactions. An apparent dissociation constant of $k_d = 43$ nM was measured for binding by WKG* -IRDye800 to SK-Hep1 cells using flow cytometry, Fig. 3D. An apparent association time constant of $k = 0.26\ min^{-1}$ (6.8 min) was measured to support rapid binding onset, Fig. 3E. The flow cytometry results at individual time points are shown, Fig. S8.

### 2.7. Effect of peptide on cell signaling

Western blots were performed to evaluate markers for activation of downstream cell signaling, Fig. S9. Incubation of low molecular weight hyaluronan (HA) as a positive control with SK-Hep1 cells showed strong phosphorylation activity for downstream AKT and ERK1/2, including pAKT and pERK1/2, respectively. By comparison, addition of WKG* -IRDye800 at various concentrations resulted in no change in phosphorylation of downstream substrates.

### 2.8. Cytotoxicity

An MTT assay was performed to evaluate the cytotoxicity of CD44 peptides. Peptides were incubated with SK-Hep1 cells in increasing concentrations up to 200 μg/mL for 24 h. The WKG* -IRDye800 and WYK* -IRDye800 showed no effect on cell viability until the highest concentrations were reached, Fig. S10.

### 2.9. Serum stability

To evaluate the serum stability of WKG* -IRDye800, the peptide was incubated with mouse serum up to 24 h, and then measured by analytical RP-HPLC, Fig. S11A. The relative concentration was determined by the area-under-the-peak, and a half-life of $T_{1/2} = 5.1$ h was measured, $R^2 = 0.99$, Fig. S11B.

### 2.10. In vivo photoacoustic imaging of orthotopic human HCC xenograft tumors

Photoacoustic images were collected in vivo from the human SK-Hep1 HCC xenograft tumors implanted orthotopically in mouse liver to evaluate the time course for peptide uptake, Fig. 4A. Minimal intensity was observed from the tumors prior to peptide injection (0 hr). Following intravenous administration of WKG* -IRDye800, the intensity peaked at 1.75 h post-injection, and returned to baseline by ~24 h. Unlabeled WKG* (7 mM, 200 μL) was injected 20 min prior to WKG* -IRDye800 to compete for binding to CD44. Decreased signal was observed from the tumors over time. WYK* -IRDye800 was administered systemically for control, and showed reduced intensity. Indocyanine green (ICG) was also administered (2.46 mg/kg) for comparison. Peak uptake of ICG was not observed within 24 h post-injection. $T_1$-weighted MR images were collected from tumor-bearing mice to confirm

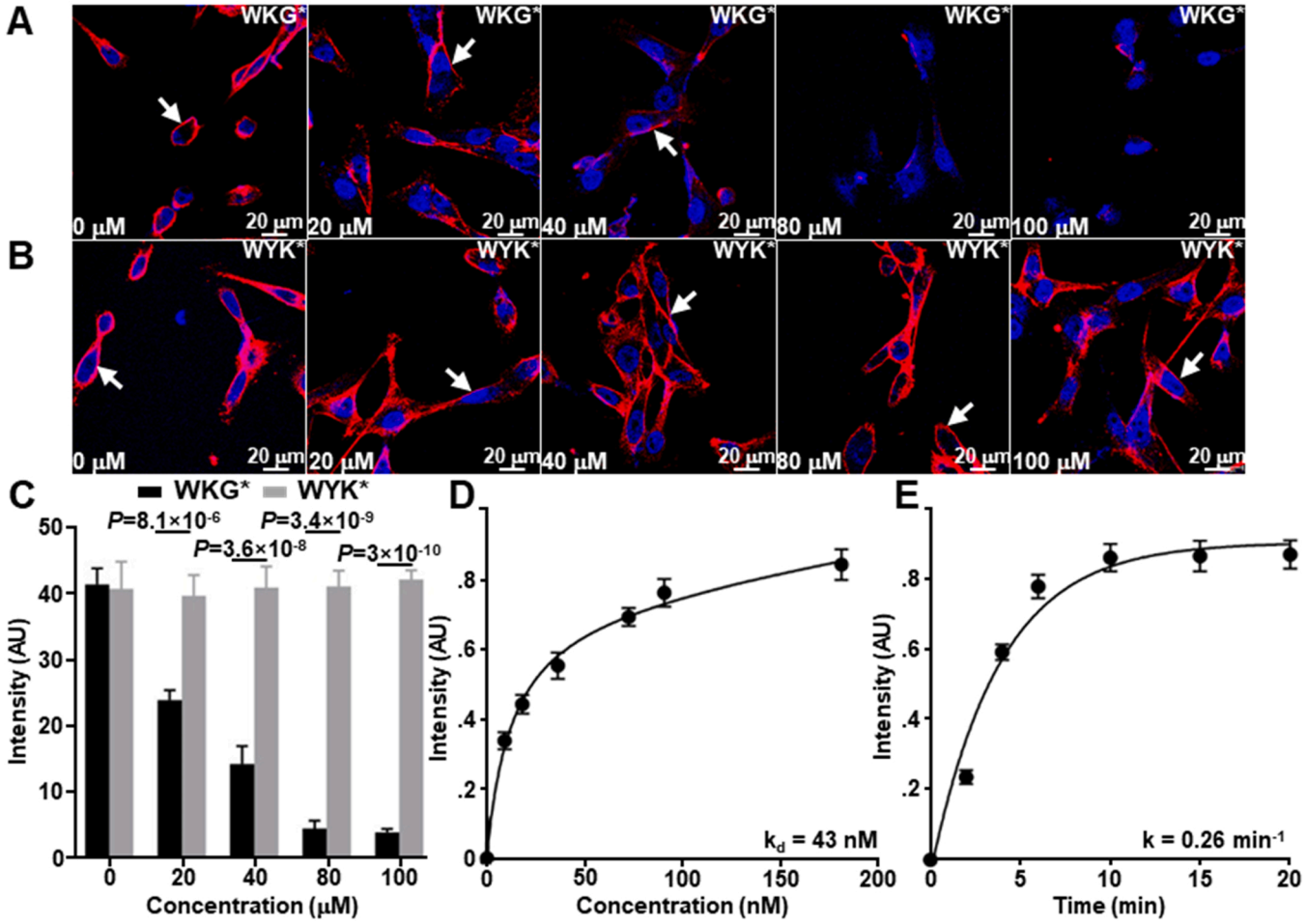


**Fig. 3.** Characterization of peptide binding parameters. (A) Binding by WKG* -IRDye800 (red) to SK-Hep1 human HCC cells decreases significantly with competition from unlabeled WKG* but not with addition of (B) WYK* (control). (C) Quantified fluorescence intensities show a concentration-dependent reduction, with significantly lower intensity when unlabeled WKG* is added relative to an equal concentration of WYK* (1.02, 0.61, 0.36, 0.12, and 0.10-fold change, respectively). (D) An apparent dissociation constant of $k_d = 43$ nM, $R^2 = 0.99$, is measured for binding of WKG* -IRDye800 to SK-Hep1 cells. (E) An apparent association time constant $k = 0.26$ min$^{-1}$ (6.8 min), $R^2 = 0.95$, is measured. Results are representative of 3 independent experiments.

the presence of orthotopically implanted HCC tumor (arrow), Fig. 4B. A 3D reconstruction shows the tumor dimensions, Fig. 4C. Quantified intensities confirm peak uptake of WYK* -IRDye800 in tumor at 1.75 h post-injection, and returned to baseline by ~24 h Fig. 4D. The mean T/B ratio for WKG* was found to be significantly greater than that for block, WYK* , and ICG at peak uptake, Fig. 4E.

### 2.10.1. *In vivo whole body imaging of orthotopic human HCC xenograft tumors*

Whole body fluorescence images collected from orthotopic SK-Hep1 xenograft tumors showed minimal intensity prior to peptide injection (0 hr), Fig. 5A. Following intravenous administration of WKG* -IRDye800, the intensity peaked at 1.75 h post-injection, and returned to baseline by ~24 h. Unlabeled WKG* (7 mM, 200 μL) was injected 20 min prior to WKG* -IRDye800 to compete for binding to CD44 (block), and decreased fluorescence intensities were observed from the tumors at each time point. WYK* -IRDye800 was administered systemically for control, and showed reduced intensity. ICG was also administered as a comparison, and showed strong background up to 24 h. Quantified intensities confirmed peak uptake of WYK* -IRDye800 in tumor at 1.75 h post-injection, and returned to baseline by ~24 h Fig. 5B. The mean T/B ratio for WKG* was found to be significantly greater than that for block, WYK* , and ICG at peak uptake, Fig. 5C.

### 2.11. *Laparoscopic imaging of orthotopic human HCC xenograft tumors*

WKG* -IRDye800, unlabeled WKG* (block), WYK* -IRDye800, and ICG were administered systemically 1.75 h prior to imaging. A conventional surgical laparoscope was attached to a custom imaging module to collect white light (WL) and NIR fluorescence (FL) images. Representative white light images collected laparoscopically are shown, Fig. 6A-D. Fluorescence image collected at 1.75 h post-injection of WKG* -IRDye800 showed qualitatively greater intensity than that for WYK* -IRDye800 (control), WKG* (block), and ICG, respectively. Ultrasound (US) and $T_1$-weighted MR images confirm the orthotopic location of the implanted HCC tumors (arrow), Fig. 6E,F. Image intensities were quantified, and the mean T/B ratio for WKG* was significantly greater than that for block, WYK* , and ICG, Fig. 6G. After completion of imaging, the mice were euthanized, and the livers were resected. A human specific anti-cytokeratin was stained on tumor sections by IHC to further confirm the implanted human derived HCC tumors, Fig. 6H. Overexpression of CD44 was confirmed by IHC and IF, Fig. 6I,J. Representative histology (H&E) of the tumor is shown, Fig. 6K.

### 2.12. *Peptide biodistribution*

Tumor-bearing mice were sacrificed at 1.75 h post-injection of WKG* -IRDye800, WYK* -IRDye800, WKG* , and ICG. White light and NIR fluorescence images were collected from major organs, Fig. S12.

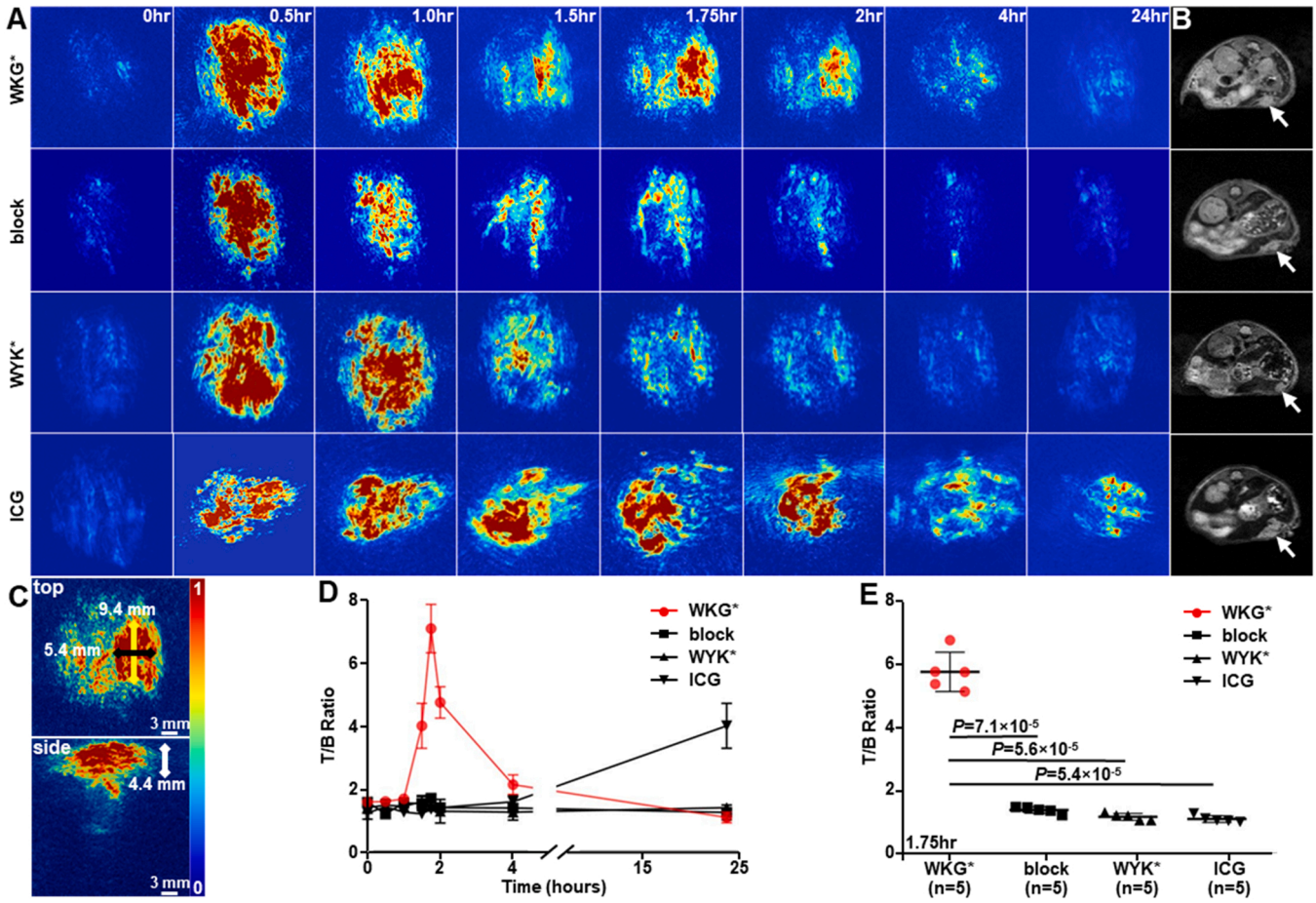


**Fig. 4.** In vivo photoacoustic imaging. (A) Images of orthotopic human HCC xenograft tumors (SK-Hep1) were collected with excitation at $\lambda_{ex} = 774$ nm before (0 h) and at 0.5, 1, 1.5, 1.75, 2, 4, and 24 h after intravenous injection of WKG* -IRDye800. After transient changes, the intensity peaks at 1.75 h. Photoacoustic images are shown for unlabeled WKG* was injected 20 min prior to WKG* -IRDye800 to compete for binding (block), WYK* -IRDye800, and ICG. (B) MR images confirm orthotopic location of the HCC tumors (arrows). (C) Representative 3D photoacoustic image reconstruction of the tumors are shown at 1.75 h post-injection with a width 5.4 mm, length 9.4 mm (top view) and depth 4.4 mm (side view). (D) The quantified T/B ratio confirms peak uptake of WKG* -IRDye800 by tumor at 1.75 h. Block and WYK* -IRDye800 displayed reduced signal over 24 h. The intensity from ICG was low early and increased gradually over 24 h. (E) At 1.75 h post-injection, the quantified T/B ratio for WKG* -IRDye800 was significantly greater than those of block, WYK* -IRDye800, and ICG (mean±SD: 7.12 ± 0.77, 1.74 ± 0.13, 1.47 ± 0.13, and 1.39 ± 0.13, respectively, n = 5 mice were evaluated for each group). The adjacent non-tumor tissue region with equal area to the tumor region was used for background.

Uptake of WKG* -IRDye800 in the tumor was found to be significantly higher versus that of other groups. For WYK* and WKG* , low uptake was observed in all other organs except the kidneys where the peptide is cleared. ICG showed strong signal from stomach and intestine due to the different route of body clearance.

### 2.13. Animal necropsy

After systemic administration of WKG* -IRDye800 for 48 h, normal healthy mice were sacrificed, vital organs and blood were collected. Acute peptide toxicity on vital organs were evaluated by histology. No signs of toxicity were seen in heart, liver, spleen, lung, kidney, stomach, intestine and brain, Fig. S13A. Whole blood and serum were collected for evaluation of hematology and chemistry, and no acute peptide toxicity was observed, Fig. S13B.

### 2.14. Peptide validation in human HCC specimens ex vivo

A tissue microarray (TMA) of n = 89 specimens was prepared to evaluate specific binding of the CD44 peptide to human HCC. Immunofluorescence staining on HCC, cirrhosis, adenoma, and normal were performed with WKG* -IRDye800 (red) and anti-CD44-AF488 (green). Both peptide and antibody showed intense staining for HCC, Fig. 7A. Minimal staining to adenoma and moderate diffuse staining to cirrhosis were observed, Fig. 7B,C. A representative section of normal human liver showed negligible staining, Fig. 7D. Results were compared with histology interpreted by an expert liver pathologist (EKC). The fluorescence intensities were quantified, and the mean (±SD) values were significantly greater for HCC than for the other histological classifications, Fig. 7E. The ROC curve shows 87% sensitivity and 69% specificity for distinguishing HCC from cirrhosis with AUC = 0.79, Fig. 7F, and 87% sensitivity and 79% specificity for distinguishing HCC from benign (cirrhosis, adenoma, and normal) with AUC = 0.87, Fig. 7G.

## 3. Methods

### 3.1. Ethics approvals

All experimental procedures were performed in compliance with relevant regulations of the University of Michigan. Mice were housed per guidelines of the Unit for Laboratory Animal Medicine (ULAM), and in vivo imaging was performed with approval by the University of Michigan Committee on the Use and Care of Animals (UCUCA). All patient reports and human tissues were deidentified prior to the study.

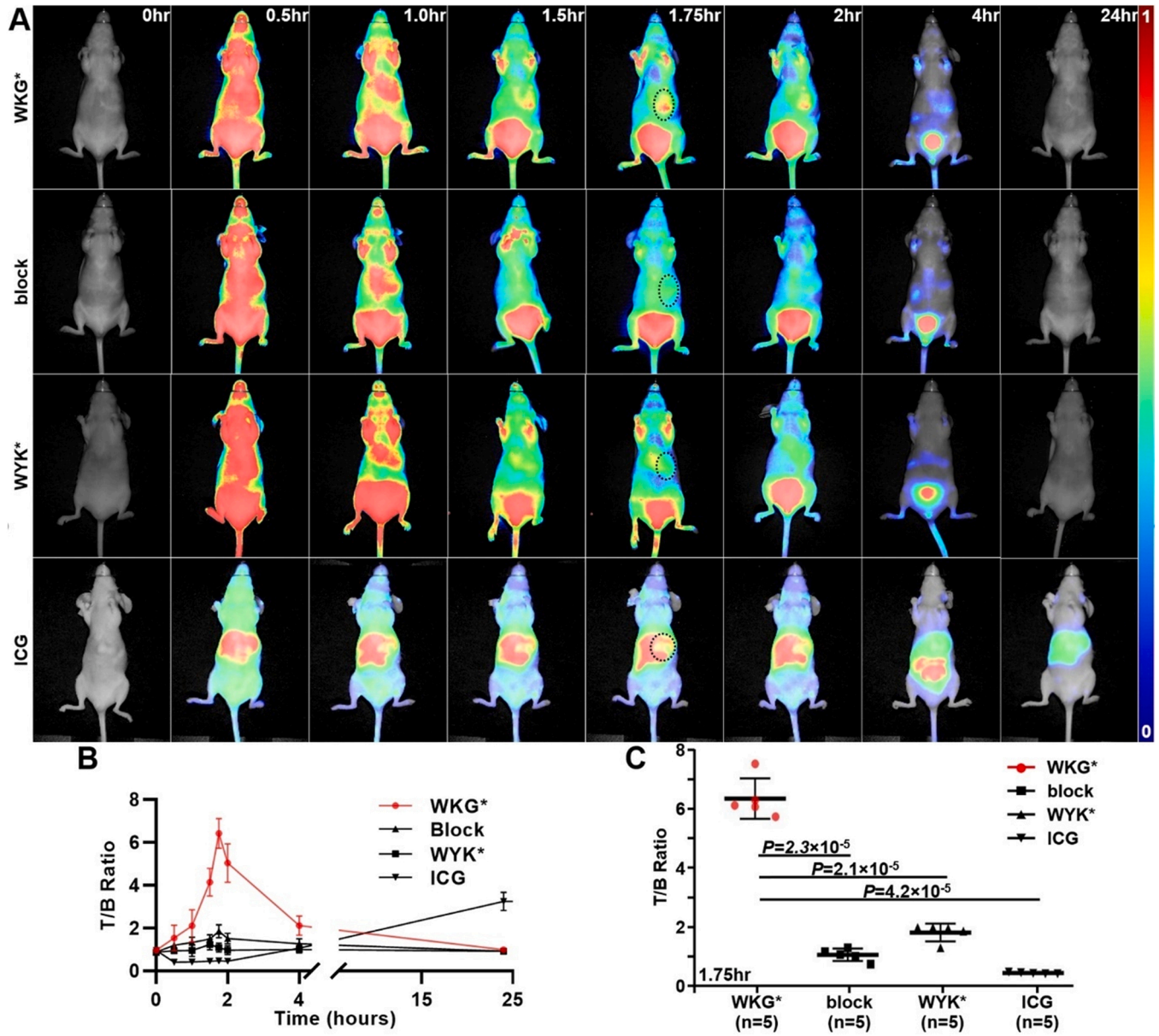


**Fig. 5.** In vivo whole body fluorescence imaging. (A) Whole body fluorescence images were collected with excitation at $\lambda_{ex} = 800$ nm before (0 h) and at 0.5, 1, 1.5, 1.75, 2, 4, and 24 h after intravenous injection of WKG* -IRDye800. Unlabeled WKG* , injected 20 min prior to WKG* -IRDye800 to compete for binding (block), and WYK* -IRDye800 showed reduced values over 24 h. The result for ICG (control) was low initially, but increased over time. Peak signals at 1.75 h from the site of the tumors (circle) support the photoacoustic results. Minimal signal was seen from the kidneys until 4 h because of their posterior location with mice placed in the supine position. (B) The quantified T/B ratio confirms a peak uptake of WKG* -IRDye800 by tumor at 1.75 h. The adjacent non-tumor tissue region with equal area to the tumor region was used for background. (C) The quantified T/B ratio for WKG* -IRDye800 was significantly greater than those of block, WYK* -IRDye800, and ICG (mean±SD: 6.42 ± 0.69, 1.09 ± 0.21, 1.85 ± 0.30, and 0.46 ± 0.03, respectively, n = 5 mice were evaluated for each group). The adjacent non-tumor liver tissue region with equal area to the tumor region was used for background.

### 3.2. Cells lines, culture media, and chemicals

Human SK-Hep1 and Hep3B hepatocellular carcinoma (HCC) cells were obtained from the American Type Culture Collection (ATCC), and cultured in Eagle's minimum essential medium (EMEM), supplemented with 10% fetal bovine serum (FBS, heat inactivated), 1% sodium pyruvate, and 1% EMEM non-essential amino acids solution. The cells were cultured at 37 °C under a humidified atmosphere with 5% $CO_2$. All media and reagents were obtained from Gibco.

Fmoc-amino acids, Boc amino acids, o-benzotriazole-N,N,N′,N′-tetramethyluronium hexafluorophosphate (HBTU), and 1-hydroxybenzotriazole (HOBt) were obtained from Aapptec and AnaSpect. Rink amide MBHA resin was procured from Novabiochem. Acetonitrile, dichloromethane (DCM), N,N-Dimethylformamide were purchased from Thermo Scientific. IRDye800CW maleimide was obtained from LI-COR Biosciences. All chemicals were of analytical grade, and used without further purification.

### 3.3. Peptide specific for CD44

A library of candidate peptide sequences was formed by analyzing a contact map for binding activity to the extracellular hyaluronan binding domain of CD44s (1UUH). CABS-dock [34,35] was used to explore possible peptide binding sites and to evaluate alignment. This software enables full flexibility of the peptide structure and large-scale flexibility of protein fragments during an empiric search for binding sites. Pairs of

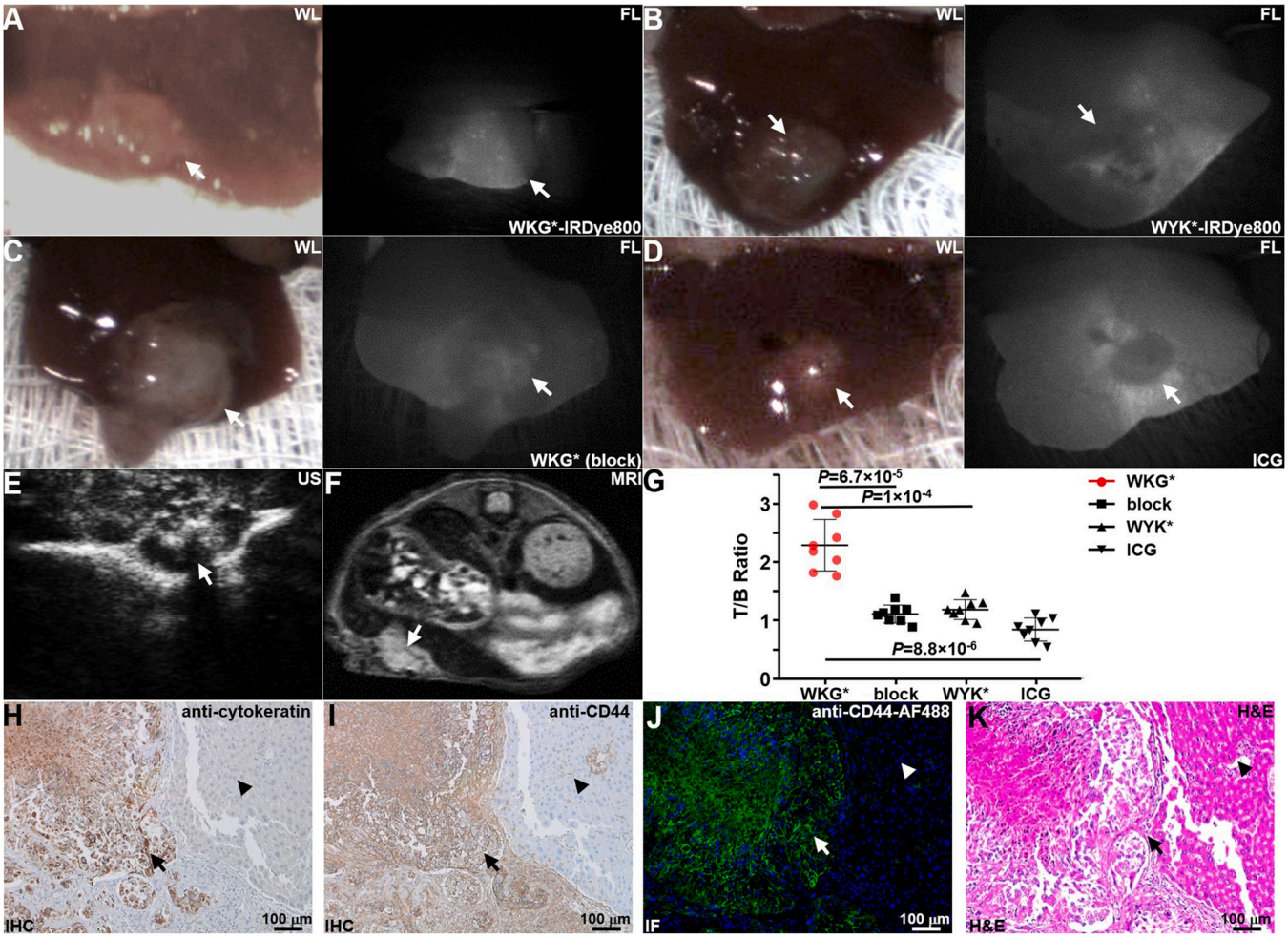


**Fig. 6.** In vivo laparoscopic fluorescence imaging. Representative white light (WL) and fluorescence (FL) images collected in vivo are shown at 1.75 h post-injection of (A) WKG* -IRDye800, (B) WYK* -IRDye800 (control), (C), WKG* (block), and (D) ICG. Representative (E) ultrasound (US) and (F) $T_1$-weighted MR images confirm orthotopic location of human HCC xenograft tumors (arrows). (G) The mean T/B ratio for WKG* -IRDye800 was significantly greater than that for WKG* (block), WYK* -IRDye800, and ICG (mean±SD: 2.32 ± 0.44, 1.13 ± 0.15, 1.21 ± 0.17, and 0.87 ± 0.2, respectively), n = 8 mice were evaluated in each group. Background was defined as the adjacent non-tumor region with equal area of the tumor region. Immunohistochemistry (IHC) using (H) human-specific anti-cytokeratin and (I) anti-CD44 shows presence of HCC xenograft tumor (arrow) adjacent to mouse liver (arrowhead) to confirm orthotopic location. (J) Immunofluorescence (IF) of adjacent section supports this result. (K) Histology (H&E) from adjacent section is shown.

peptide/target residues with inter molecular distance < 4.5 Å were generated to optimize binding affinity and specificity [34]. Amino acids that paired more than 5 times were recognized as having high correlation and affinity, and was preserved in the sequence. The general peptide sequence WX1×2WX3×4X5×6TX7×8A was used where X1 represents either H or K to form hydrophilic interactions with CD44 at the N-terminus. X2 represents either P or G which often form "turns" of peptides. On sites X3-X6, amino acids with different properties were chosen to increase sequence diversity. X3 represents S or N; X4 represents Y, A, I or F; X5 represents L, A, I or F; X6 represents W, A, I or F. X7-X8 at the C-terminus represents negative charged Q or D which have an electrostatic repulsion to the negative extraneous coat of cells to reduce peptide entry into the cells. In the library, from X1-X8, the sequence was randomly distributed, resulting in a complexity of $2 \times 2 \times 2 \times 4 \times 4 \times 4 \times 2 \times 2 = 2048$. We used Hex 8.0.0 protein-ligand docking software to evaluate binding of each candidate peptide to the CD44 hyaluronan binding domain [41]. This program comprehensively evaluates all possible combinations for the predicted binding motifs of each candidate sequence, and calculates the docking energy for binding between the peptide and target. Hex 8.0.0 was also used to identify a scrambled sequence for use as control.

### 3.4. Peptide synthesis

The target and control peptides were synthesized using standard Fmoc-mediated solid-phase chemical synthesis on rink amide MBHA resin using a PS3 automatic synthesizer (Protein Technologies Inc). Fmoc (Fluorenylmethyloxycarbonyl) and Boc (Butyloxycarbonyl) protected *L*-amino acids were used with standard HBTU/HOBt activation. After assembly, the resin was washed with dimethylformamide (DMF) and dichloromethane (DCM), cleaved with a trifluoroacetic acid cocktail (TFA: thioanisole: phenol : EDT: H2O, 87.5:5:2.5:2.5:2.5, v/v/v/v/v). The resulting peptide was precipitated in − 20 °C diethyl ether. The crude peptides were then purified using reversed-phase high performance liquid chromatography (RP-HPLC). The purified peptide was lyophilized to produce a white powder, and was characterized with MALDI-TOF mass spectrometry.

### 3.5. Spectral measurements

The absorbance spectrum of peptides was measured using a UV-Vis spectrophotometer (NanoDrop 2000c, Thermo Scientific). The peptides were excited at $\lambda_{ex}$ = 785 nm with a single-mode diode laser (#iBEAM-SMART-785-S, Toptica Photonics), and FL emission was

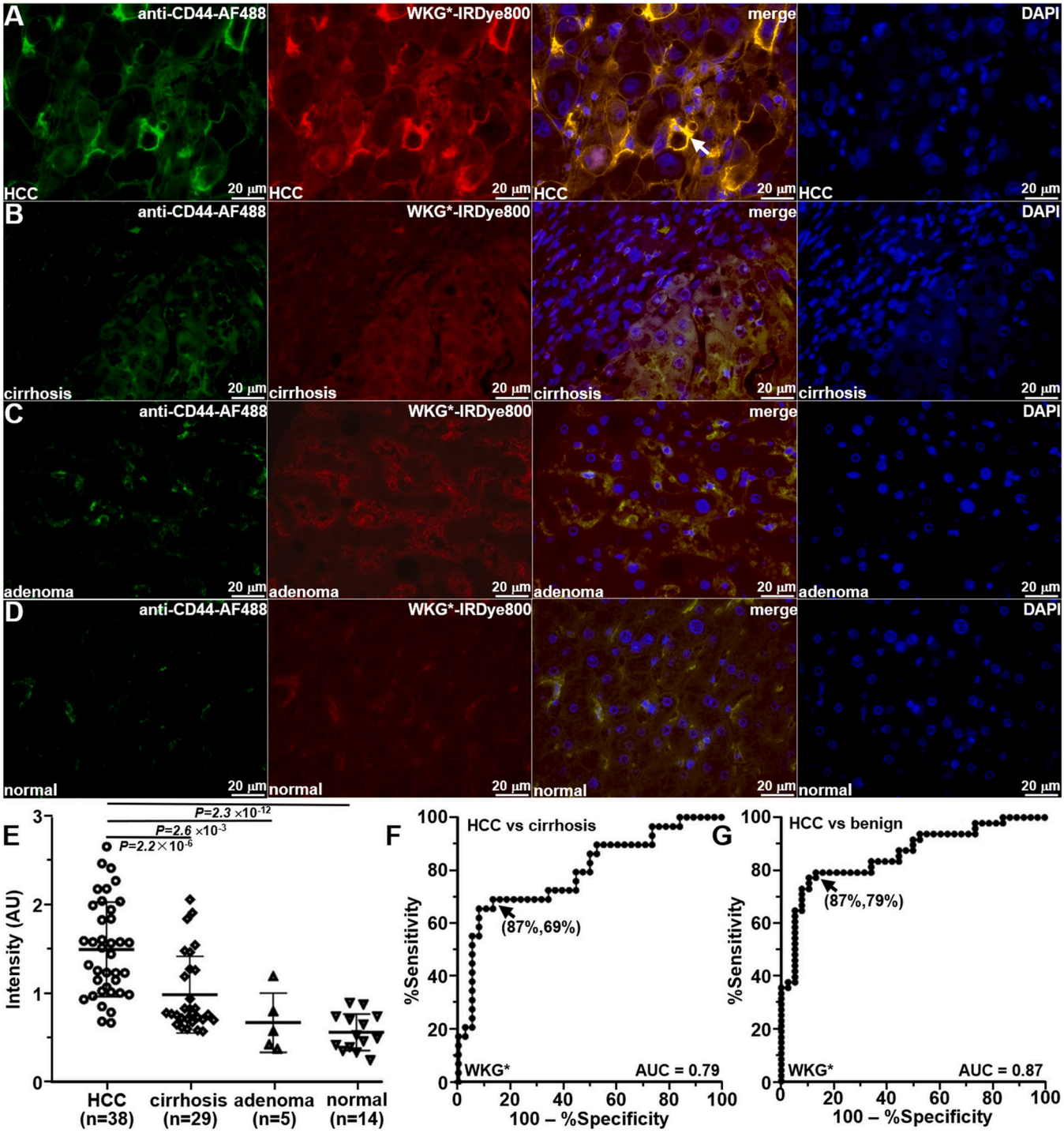


**Fig. 7.** Specific peptide binding to human HCC ex vivo. (A) WKG* -IRDye800 (red) and anti-CD44-AF488 (green) show strong binding to the cell surface (arrows) of HCC using immunofluorescence. (B) Diffuse signal is observed for cirrhosis. (C) Mild staining is seen with peptide and antibody to hepatic adenoma. (D) Minimal intensity is seen for normal human liver. (E) Quantified fluorescence intensities show that the intensities associated with HCC is significantly greater than those for adenoma, cirrhosis, and normal human liver (mean ± SD: 1.47 ± 0.50, 0.93 ± 0.35, 0.67 ± 0.34, and 0.56 ± 0.21, n = 86 human specimens were evaluated). (F) ROC curve shows 87% sensitivity and 69% specificity for WKG* -IRDye800 to distinguish HCC from cirrhosis with an AUC = 0.79. (G) ROC curve shows 87% sensitivity and 79% specificity to distinguish HCC from benign (cirrhosis, adenoma, and normal) with AUC = 0.87.

collected using a UV-Visible-NIR spectrometer (USB2000 +, Ocean Insight). The spectra were plotted using Prism 5.0 software (GraphPad Inc).

### 3.6. siRNA knockdown

CD44 expression in SK-Hep1 cells was knocked down using 3 different siRNAs, including (1) L-009999–00–0005, Dharmacon; (2) s2681, Thermo Fisher; and (3) 106160, Thermo Fisher. MISSION® siRNA Universal Negative Control (SIC001, Sigma) was used for control. Cells were transfected with Lipofectamine 2000 (11668027, Invitrogen) per manufacturer instructions, and then incubated with 4 μM of peptide for 3 min. A 1:3000 dilution of rabbit anti-CD44 antibody (EPR18668, Abcam) was used for positive control. CD44 expression was determined

by Western blot within 72 h.

### 3.7. Confocal fluorescence microscopy

$\sim 10^3$ SK-Hep1 and Hep 3B cells were grown on cover glass in 24-well plate to ~70% confluence. The cells were washed with PBS 1X and incubated with 4 μM of either target or control peptide for 3 min. The cells were then washed 3X in PBS, fixed with 4% paraformaldehyde (PFA) for 8 min, washed 3X with PBS then incubated with 2% BSA, 1% goat serum in PBS for 30 min. The cells were incubated with a 1:3000 dilution of primary recombinant rabbit anti-CD44 antibody (#ab189524, Abcam) for 30 min on ice and then incubated with a 1:500 dilution of AF488-labeled secondary goat ant-rabbit immunoglobulin G antibody (#A-11029, Life Technologies) for 12 h at 4 °C, and then mounted on glass slides with ProLong Gold reagent containing DAPI (Invitrogen). Confocal fluorescence images were collected on Leica SP8 confocal microscope using a 63X oil-immersion objective. Fluorescence intensities were quantified using custom MATLAB (Mathworks) software.

### 3.8. Peptide characterization

Specific peptide binding to CD44 was further validated using competitive inhibition by adding unlabeled peptide. $\sim 10^3$ SK-Hep1 cells were grown to ~70% confluence on cover glass in triplicate. Unlabeled peptides at concentrations of 0, 10, 20, 40, 80, and 100 μM were incubated with the cells for 30 min at 4 °C. The cells were washed with PBS and incubated with 5 μM of the target peptides for another 30 min at 4 °C. The cells were washed and fixed with 4% PFA for 8 min. The cells were washed with PBS and mounted with ProLong Gold reagent containing DAPI (Invitrogen).

The apparent dissociation constant $k_d$ for peptide binding to cells was measured to assess the binding affinity [42]. IRDye800-labeled target peptides were serially diluted in PBS at concentrations of 0, 10, 20, 40, 80, 100, and 200 nM. $\sim 10^5$ SK-Hep1 cells were incubated with the peptides at 4 °C for 1 h, washed with cold PBS, and the mean fluorescence intensities were measured using flow cytometry. The equilibrium dissociation constant $k_d = 1/k_a$ was calculated by performing a least squares fit of the data to the non-linear equation $I = (I_0 + I_{max} k_a [X])/(I_0 + k_a[X])$. $I_0$ and $I_{max}$ are the initial and maximum fluorescence intensities, corresponding to no peptide and at saturation, respectively, and [X] represents the concentration of the bound peptide. Prism 5.0 software (GraphPad Inc) was used to calculate $k_d$.

The apparent association time constant *k* was measured by incubating $\sim 10^6$ SK-Hep1 cells with 5 μM IRDye800-labeled peptides for time intervals ranging between 0 and 20 min at 4 °C. The cells were centrifuged and washed with cold PBS. The cells were fixed with 4% PFA for 30 min at 4 °C before analyzing with flow cytometry. The rate constant *k* was calculated by fitting the data to a first-order kinetics model $y(t) = I_{max}[1 - \exp(-kt)]$, where $I_{max}$ is the maximum value using Prism 5.0 software (GraphPad).

### 3.9. Effect of peptide on cell signaling

SK-Hep1 cells were incubated with either hyaluronan (HA) or peptide to evaluate activation of downstream signaling after binding to CD44. 100 μg/mL of low molecular weight HA (GLR001, R&D Systems) was added for 15 min. Peptides are added at concentrations of 4 and 300 μM for 15 min. Anti-CD44 antibody (#ab189524, Abcam), anti-AKT (#4691, Cell Signaling), anti-phospho-AKT (#9271, Cell Signaling), anti-ERK1/2 (#ab17942, Abcam,), anti-phospho-ERK1/2 (#ab50011, Abcam), and anti-β-Actin (#4967, Cell Signaling Technology) were used per manufacturer's instructions.

### 3.10. Cytotoxicity

The target and control peptides were serially diluted over a range of concentrations and incubated with SK-Hep1 cells seeded in 96-well plates for 24 h. The media was then removed, and MTT solution (100 μL, 0.5 mg/mL) was added. After 4 h for incubation, the MTT solution was removed, and 150 μL of DMSO was added to each well to solubilize formazan crystals produced by living cells. Absorbance at $\lambda_{abs} = 570$ (test) and 630 nm (reference) was measured using a plate reader (VersaMax™ Tunable Microplate Reader). The half-maximum inhibitory concentration ($IC_{50}$) was measured.

### 3.11. Serum stability

Serum stability was evaluated by dispersing 30 μM of peptide in mouse serum and incubating at 37 °C for 0, 0.5, 1, 2, 4, 8 and 24 h. Serum stability was monitored by HPLC. The relative peptide concentrations were determined by measuring the area under the peak (Breeze 2, Waters).

### 3.12. Orthotopic HCC mouse model

Human HCC xenograft tumors were implanted orthotopically in female nude athymic mice. First, $\sim 5 \times 10^6$ SK-Hep1 cells were injected subcutaneously into the hind limb flank. Tumors were then monitored twice a week and allowed to grow to 1–2 cm in diameter for 10–30 days. A small horizontal incision was made below the sternum to expose the liver. The liver was incised with a sharp scalpel horizontally in parallel with the surface of the exposed liver. A piece of the subcutaneous tumor with dimensions of $\sim 1 \times 1 \times 1$ mm$^3$ was implanted into the incision, and then the site was sealed with absorbable hemostatic material (surgical, Johnson & Johnson). The liver was returned to its original position after confirming hemostasis.

#### 3.12.1. In vivo photoacoustic imaging of orthotopic human HCC xenograft tumors

IRDye800-labeled target and control peptides (300 μM in 200 μL PBS) were intravenously injected in mice bearing orthotopical SK-Hep1 tumors. An unlabeled peptide (1.5 mM, 100 μL) was injected 30 min prior to the labeled peptide to compete for binding. ICG (2.46 mg/kg) was injected intravenously as a control. Three-dimensional (3D) images were acquired from 0 to 48 h post injection and reconstructed using PAI tomography system (Nexus 128, Endra) using $\lambda_{ex} = 774$ nm excitation. The photoacoustic signal intensity was measured from the two-dimensional (2D) maximum intensity projection (MIP) images, and the pre-injection images were used for background.

#### 3.12.2. In vivo whole body imaging of orthotopic human HCC xenograft tumors

SK-Hep1 tumor bearing mice were injected intravenously with the IRDye800-labeled target and control peptides (300 μM in 200 μL PBS). Unlabeled peptide and ICG were administrated as above. The spatial extent and margins of tumors were identified using a NIR whole body fluorescence imaging system (Pearl®, LI-COR Biosciences) up to 24 h post injection. The images were acquired using $\lambda_{ex} = 800$ nm with 85 μm resolution and $16.8 \times 12$ cm$^2$ field of view (FOV). Image Studio software (Li-Cor Biosciences) was used for analysis. Regions of interest (ROI) with area equal to that of the tumor and adjacent in location was measured for background.

### 3.13. Laparoscopic imaging of orthotopic human HCC xenograft tumors

A self-build imaging module was attached to standard surgical laparoscope (#49003 AA, HOPKINS II Straight Forward Telescope 0°, Karl Storz, El Segundo, CA, USA) to collect WL and NIR FL images. WL illumination (MCWHL5, Thorlabs, Newton, NJ, USA) and FL excitation

source ($\lambda_{ex}$ = 785 nm, #iBEAM-SMART-785-S, Toptica Photonics) were coupled into the laparoscope. WL and NIR FL images are collected, simultaneously, by a color CCD camera (#GX-FW-28S5C-C, Point Gray Research, Richmond, BC V6W 1K7, Canada) and a NIR CCD camera (Orca R-2, Hamamatsu Photonics, Hamamatsu City, Shizuoka Pref., Japan) with a laser power of 1.2 mW, respectively.

### 3.14. Peptide biodistribution

The animals were euthanized at peak uptake after intravenous injection of the target and control peptides as above. Unlabeled peptide and ICG were administrated as above. Major organs, including heart, spleen, lung, liver, brain, stomach, kidney, intestine, were resected and exposed for white light and fluorescence imaging to measure peptide biodistribution.

### 3.15. Animal necropsy

Mice were euthanized 48 h post-injection with WKG* -IRDye800 (300 μM in 200 μL PBS). Whole blood was collected for chemistry. Liver, kidney, heart, lung, spleen, stomach, intestine, and brain were harvested and submitted for routine histology (H&E). All slides were evaluated by a liver pathologist.

### 3.16. Peptide validation in human HCC specimens ex vivo

A tissue microarray (TMA) of human HCC was generated to investigate specific binding by the CD44 peptide to human HCC. Formalin-fixed, paraffin-embedded (FFPE) sections of human liver were obtained from the archived tissue bank in the Department of Pathology. The specimens were washed 3X in xylene for 3 min, 100% ethanol for 3 min, 95% ethanol for 3 min, 70% ethanol for 3 min, rinsed in $H_2O$ for 2 min. Antigen unmasking was performed by boiling the slides in 10 mM sodium citrate buffer with 0.05% Tween at pH 6.0 for 15 min. The slides were cooled to RT, and were washed in $H_2O$ 3X for 5 min. Blocking was performed with DAKO protein blocking agent (X0909, DAKO) for 1 h at RT. The peptides at 1 μM concentration were incubated for 10 min at RT. The sections were washed 3X in PBST for 3 min, and incubated with 400 μL at 1:500 dilution of recombinant anti-CD44 (#ab189524, Abcam) overnight at 4 °C. The sections were then washed 3X in PBST for 5 min. A 1:500 dilution of AF488-labeled secondary antibody (goat anti rabbit Alexa Fluor® 488) was added to each section and incubated for 1 h at RT. The secondary antibody solution was removed and washed 3X with PBST for 5 min. The sections were then mounted with ProLong Gold reagent containing DAPI (Invitrogen). The fluorescence images of each specimen were collected using confocal microscopy (SP8, Leica), and the mean fluorescence intensity from each image was measured from 3 boxes with dimensions of 20 × 20 $\mu m^2$ using custom MATLAB software. Regions of saturated image intensities were avoided.

### 3.17. Statistical analysis

Two-sided Welch's two-sample *t*-tests were performed to assess the specific binding of WKG* to HCC cells, which allow unequal variance in the two groups being compared. All tests were performed at the Bonferroni-corrected significance level $\alpha = 0.05/m$, where m is the total number of statistical tests performed, to account for the multiple comparisons made between WKG* and various controls. For example, if 3 controls are present, each individual test would be performed at $\alpha = 0.05/3 = 0.017$, and if 3 controls were examined in 9 tissues, each target peptide versus control test would be performed at $\alpha = 0.05/27 = 0.0019$.

## 4. Discussion

We used a structural model for the extracellular hyaluronan binding domain of CD44s (1UUH) to optimize the sequence of a 12-mer peptide for specific binding to CD44. The peptide was labeled with IRDye800, and specific binding was validated in vitro with knockdown, competition, and co-localization assays. Binding properties were characterized by an apparent dissociation constant of $k_d$ = 43 nM and apparent association time constant of k = 0.26 $min^{-1}$ (6.8 min). Human HCC cells were implanted orthotopically in mouse liver, and peak uptake in vivo by xenograft tumors was observed at 1.75 h post-injection using photoacoustic imaging. Specific peptide uptake by tumor was supported by fluorescence images collected in vivo using whole body and laparoscopic methods. Specific peptide binding to CD44 in vivo was further confirmed by blocking the targeted contrast agent with competition from unlabeled peptide. Ex-vivo staining results using human HCC specimens support the ability of this peptide to distinguish HCC from other liver pathologies. No evidence of toxicity was observed on animal necropsy.

Previous peptides specific for CD44 have been reported. A peptide was selected using biopanning with a M13 phage display library for detection of breast cancer [43]. A binding affinity of 115.8 and 256.5 nM was measured for FITC-labeled and biotinylated peptides, respectively. No in vivo imaging was performed. A peptide specific for CD44 was developed for early detection of gastric cancer [44]. Docking to CD44 was evaluated using a structural model, and a binding affinity of $k_d$ = 135.1 nM was reported. Fluorescence imaging was performed in subcutaneous gastric tumors, and a peak T/B ratio in tumor was detected 3 h post-injection. The biodistribution showed accumulation in both tumor and liver. Also, a peptide specific for CD44v6 was identified, and a binding affinity of $k_d$ = 611.2 nM was reported [45]. By comparison, our peptide showed much improved binding affinity, and demonstrated primarily renal clearance. This mechanism results in reduced background that can limit imaging performance.

Recently a multi-modal theranostic platform combing photoacoustic, fluorescence, and MR imaging has been evaluated in HCC [46]. We used multi-modal imaging methods to rigorously validate specific peptide binding to CD44 in vivo. First, ultrasound and MRI were used to confirm the orthotopic location of HCC tumors. Photoacoustic and fluorescence imaging methods provide different physical mechanisms by which signal is generated from the NIR-labeled peptide to confirm specific ligand binding to the CD44 target. The photoacoustic images combine light with sound to visualize the depth of peptide accumulation in tumor. The whole body fluorescence images demonstrated the spatial distribution of peptide uptake by tumor in comparison with other body organs. Both modalities showed peak tumor uptake at 1.75 h post-injection, and clearance by ~24 h. Fluorescence laparoscopy was performed intraoperatively, and demonstrated sharp tumor margins within liver parenchyma. The peptide was found to be stable in serum for over 5 h, a time frame compatible with diagnostic imaging.

Image-guided surgery is being used with greater frequency to more precisely resect HCC tumors. Early liver micrometastasis can be detected and resected by photoacoustic image-guided surgery [47]. The intraoperative diagnosis of small tumors, especially those with indistinct margins, remains an important challenge for HCC resection. A specific targeting agent has potential to improved tumor visualization during resection to achieve a better balance between complete tumor resection and maintenance of liver function. The remaining volume of "normal" liver parenchyma needed to optimize post-operative function can then be maximized. Experienced surgeons can achieve very good patient outcomes with 5-year survival rates over 70% for solitary early-stage HCC [48–50]. ICG is FDA-approved, and is the only contrast agent currently being used to identify liver tumors, hepatic segments, and extrahepatic bile ducts in real time during open and laparoscopic surgery [51–53]. ICG is also being used for contrast-enhanced photoacoustic imaging to evaluate liver fibrosis in mice [54]. This non-specific NIR fluorophore accumulates passively in HCC via the enhanced permeability and retention (EPR) effect [55]. Our results showed that ICG achieves peak uptake over 24 h post-injection, a time frame that is

quite long for practical clinical use. Moreover, the tumor margins using ICG appeared indistinct by comparison with that using the NIR-labeled peptide.

Targeted imaging strategies are needed to improve management of patients with HCC by providing a new approach to detect, characterize, and treat tumors. Current modalities, such as ultrasound (US), computed tomography (CT), magnetic resonance imaging (MRI), and positron emission tomography (PET) have limited ability to determine the benign versus malignant nature of small nodules $< 2$ cm in size [8]. While some progress has been made with serological markers, few advances have been made with tissue biomarkers. Most HCC tumors arise from a background of cirrhosis. Early cancer detection can be achieved by developing a sensitive method to recognize imaging biomarkers that can distinguish between HCC and non-HCC. Our ex vivo data from peptide staining of human HCC with cirrhosis showed high sensitivity and specificity, however further clinical investigation is needed. HCC has high molecular heterogeneity [56], thus biomarkers may need to be combined in a panel for effective use. We have identified and validated a peptide that binds specifically to CD44. This peptide has many properties that are promising for future clinical translation in management of patients with HCC, including early cancer detection and image-guided surgery.

## Declaration of Competing Interest

The authors declare that they have no known competing financial interests or personal relationships that could have appeared to influence the work reported in this paper.

## Acknowledgements

This study was funded in part by the National Institutes of Health U01 CA230669 (TW) and the Michigan Medicine-PUHSC Joint Institute (TW).

### *Contributors*

X.W., X.M. and T.D.W. conceived and designed the experiments X. W., X.M., T.S.C., S.F., M.L. S.J. performed the experiments L.T., H.J. contributed to image and data analysis E.K.C. reviewed pathology X.W., X.M., and T.D.W. wrote the manuscript.

## Appendix A. Supporting information

Supplementary data associated with this article can be found in the online version at doi:10.1016/j.pacs.2022.100355.

## References

[1] F. Bray, J. Ferlay, I. Soerjomataram, R.L. Siegel, L.A. Torre, A. Jemal, Global cancer statistics 2018: GLOBOCAN estimates of incidence and mortality worldwide for 36 cancers in 185 countries, CA Cancer J. Clin. 68 (6) (2018) 394–424.
[2] R.L. Siegel, K.D. Miller, A. Jemal, Cancer statistics, 2020, CA Cancer J. Clin. 70 (1) (2020) 7–30.
[3] A.F. Peery, S.D. Crockett, C.C. Murphy, J.L. Lund, E.S. Dellon, J.L. Williams, E. T. Jensen, N.J. Shaheen, A.S. Barritt, S.R. Lieber, B. Kochar, E.L. Barnes, Y.C. Fan, V. Pate, J. Galanko, T.H. Baron, R.S. Sandler, Burden and cost of gastrointestinal, liver, and pancreatic diseases in the United States: Update 2018, Gastroenterology 156 (1) (2019) 254–272, e11.
[4] K.A. Cronin, A.J. Lake, S. Scott, R.L. Sherman, A.M. Noone, N. Howlader, S. J. Henley, R.N. Anderson, A.U. Firth, J. Ma, B.A. Kohler, A. Jemal, Annual report to the nation on the status of cancer, Natl. Cancer Stat. Cancer 124 (13) (2018) 2785–2800.
[5] S.K. Asrani, H. Devarbhavi, J. Eaton, P.S. Kamath, Burden of liver diseases in the world, J. Hepatol. 70 (1) (2019) 151–171.
[6] A. Ozakyol, Global epidemiology of hepatocellular carcinoma (HCC Epidemiology), J. Gastrointest. Cancer 48 (3) (2017) 238–240.
[7] A. Singal, M.L. Volk, A. Waljee, R. Salgia, P. Higgins, M.A. Rogers, J.A. Marrero, Meta-analysis: surveillance with ultrasound for early-stage hepatocellular carcinoma in patients with cirrhosis, Aliment Pharm. Ther. 30 (1) (2009) 37–47.
[8] N.C. Yu, V. Chaudhari, S.S. Raman, C. Lassman, M.J. Tong, R.W. Busuttil, D.S. Lu, CT and MRI improve detection of hepatocellular carcinoma, compared with ultrasound alone, in patients with cirrhosis, Clin. Gastroenterol. Hepatol. 9 (2) (2011) 161–167.
[9] J.M. Llovet, Y. Chen, E. Wurmbach, S. Roayaie, M.I. Fiel, M. Schwartz, S.N. Thung, G. Khitrov, W. Zhang, A. Villanueva, C. Battiston, V. Mazzaferro, J. Bruix, S. Waxman, S.L. Friedman, A molecular signature to discriminate dysplastic nodules from early hepatocellular carcinoma in HCV cirrhosis, Gastroenterology 131 (6) (2006) 1758–1767.
[10] D. Busato, M. Mossenta, L. Baboci, F. Di Cintio, G. Toffoli, M. Dal Bo, Novel immunotherapeutic approaches for hepatocellular carcinoma treatment, Expert Rev. Clin. Pharm. 12 (5) (2019) 453–470.
[11] D. Galun, T. Srdic-Rajic, A. Bogdanovic, Z. Loncar, M. Zuvela, Targeted therapy and personalized medicine in hepatocellular carcinoma: drug resistance, mechanisms, and treatment strategies, J. Hepatocell. Carcinoma 4 (2017) 93–103.
[12] Y. Luo, Y. Tan, Prognostic value of CD44 expression in patients with hepatocellular carcinoma: meta-analysis, Cancer Cell Int. 16 (2016) 47.
[13] H. Okabe, T. Ishimoto, K. Mima, S. Nakagawa, H. Hayashi, H. Kuroki, K. Imai, H. Nitta, S. Saito, D. Hashimoto, A. Chikamoto, T. Ishiko, M. Watanabe, O. Nagano, T. Beppu, H. Saya, H. Baba, CD44s signals the acquisition of the mesenchymal phenotype required for anchorage-independent cell survival in hepatocellular carcinoma, Br. J. Cancer 110 (2014) 958–966.
[14] J. Li, Y. Zhang, R. Ruan, W. He, Y. Qian, The novel interplay between CD44 standard isoform and the caspase-1/IL1B pathway to induce hepatocellular carcinoma progression, Cell Death Dis. 11 (2020) 961.
[15] K. Mima, H. Okabe, T. Ishimoto, H. Hayashi, S. Nakagawa, H. Kuroki, M. Watanabe, T. Beppu, M. Tamada, O. Nagano, H. Saya, H. Baba, CD44s regulates the TGF-β-mediated mesenchymal phenotype and is associated with poor prognosis in patients with hepatocellular carcinoma, Cancer Res. 72 (2012) 3414–3423.
[16] H.S. Ryu, S.H. Park, K.B. Lee, E. Shin, J.J. Jang, Expression of the transmembrane glycoprotein CD44s is potentially an independent predictor of recurrence in hepatocellular carcinoma, Gut Liver 5 (2011) 204–209.
[17] Z. Fan, H. Xia, H. Xu, J. Ma, S. Zhou, W. Hou, Q. Tang, Q. Gong, Y. Nie, F. Bi, Standard CD44 modulates YAP1 through a positive feedback loop in hepatocellular carcinoma, Biomed. Pharm. 103 (2018) 147–156.
[18] S. Hu, X. Wu, B. Zhou, Z. Xu, J. Qin, H. Lu, L. Lv, Y. Gao, L. Deng, J. Yin, G. Li, IMP3 combined with CD44s, a novel predictor for prognosis of patients with hepatocellular carcinoma, J. Cancer Res Clin. Oncol. 140 (2014) 883–893.
[19] K. Endo, T. Terada, Protein expression of CD44 (standard and variant isoforms) in hepatocellular carcinoma: relationships with tumor grade, clinicopathologic parameters, p53 expression, and patient survival, J. Hepatol. 32 (2000) 78–84.
[20] J. Mathew, J.E. Hines, J.O. Obafunwa, A.W. Burr, K. Toole, A.D. Burt, CD44 is expressed in hepatocellular carcinomas showing vascular invasion, J. Pathol. 179 (1996) 74–79.
[21] Z.J. Zhou, Z. Dai, S.L. Zhou, X.T. Fu, Y.M. Zhao, Y.H. Shi, J. Zhou, J. Fan, Overexpression of HnRNP A1 promotes tumor invasion through regulating CD44v6 and indicates poor prognosis for hepatocellular carcinoma, Int. J. Cancer 132 (2013) 1080–1089.
[22] M. Gudowska, B. Cylwik, L. Chrostek, The role of serum hyaluronic acid determination in the diagnosis of liver fibrosis, Acta Biochim. Pol. 64 (2017) 451–457.
[23] M. Hassn Mesrati, S.E. Syafruddin, M.A. Mohtar, A. Syahir, CD44: a multifunctional mediator of cancer progression, Biomolecules 11 (2021) 1850.
[24] D. Naor, S. Nedvetzki, I. Golan, L. Melnik, Y.J.Cricls Faitelson, CD44 Cancer 39 (6) (2002) 527–579.
[25] S.C. Ghosh, S. Neslihan Alpay, J. Klostergaard, CD44: a validated target for improved delivery of cancer therapeutics, Expert Opin. Ther. Targets 16 (7) (2012) 635–650.
[26] B. Bose, S.P. Shenoy, Stem cell versus cancer and cancer stem cell: intricate balance decides their respective usefulness or harmfulness in the biological system, J. Stem. Cell. Res. Ther. 4 (173) (2014) 2.
[27] G.M. Saed, Compositions and methods to treat solid tumors, Google Patents, 2019.
[28] H. Ponta, P.J.P.P. Herrlich, M, The CD44 protein family: roles in embryogenesis and tumor progression, Front. Biosci. 18 (4–5) (1998) 381–393.
[29] S. Lee, J. Xie, X. Chen, Peptides and peptide hormones for molecular imaging and disease diagnosis, Chem. Rev. 110 (5) (2010) 3087–3111.
[30] P. Zhang, Y. Cui, C.F. Anderson, C. Zhang, Y. Li, R. Wang, H. Cui, Peptide-based nanoprobes for molecular imaging and disease diagnostics, Chem. Soc. Rev. 47 (10) (2018) 3490–3529.
[31] W. Wang, Z. Hu, Targeting peptide-based probes for molecular imaging and diagnosis, Adv. Mater. 31 (45) (2019), e1804827.
[32] S. Feng, X. Meng, Z. Li, T.S. Chang, X. Wu, J. Zhou, B. Joshi, E.Y. Choi, L. Zhao, J. Zhu, T.D. Wang, Multi-modal imaging probe for glypican-3 overexpressed in orthotopic hepatocellular carcinoma, J. Med Chem. 64 (21) (2021) 15639–15650.
[33] A. Lo, C.T. Lin, H.C. Wu, Hepatocellular carcinoma cell-specific peptide ligand for targeted drug delivery, Mol. Cancer Ther. 7 (3) (2008) 579–589.
[34] B. Du, H. Han, Z. Wang, L. Kuang, L. Wang, L. Yu, M. Wu, Z. Zhou, M. Qian, targeted drug delivery to hepatocarcinoma in vivo by phage-displayed specific binding peptide, Mol. Cancer Res. 8 (2) (2010) 135–144.
[35] R.L. Juliano, R. Alam, V. Dixit, H.M. Kang, Cell-targeting and cell-penetrating peptides for delivery of therapeutic and imaging agents, Wiley Int. Rev. Nanomed. Nanobiotechnol. 1 (3) (2009) 324–335.
[36] M. de Serres, B. Ellis, J.E. Dillberger, S.K. Rudolph, J.T. Hutchins, C.M. Boytos, D. L. Weigl, R.B. DePrince, Immunogenicity of thrombopoietin mimetic peptide GW395058 in BALB/c mice and New Zealand white rabbits: evaluation of the

potential for thrombopoietin neutralizing antibody production in man, Stem Cells 17 (4) (1999) 203–209.
[37] S. Tangri, B.R. Mothe, J. Eisenbraun, J. Sidney, S. Southwood, K. Briggs, J. Zinckgraf, P. Bilsel, M. Newman, R. Chesnut, C. Licalsi, A. Sette, Rationally engineered therapeutic proteins with reduced immunogenicity, J. Immunol. 174 (6) (2005) 3187–3196.
[38] M. Blaszczyk, M. Kurcinski, M. Kouza, L. Wieteska, A. Debinski, A. Kolinski, S. Kmiecik, Modeling of protein–peptide interactions using the CABS-dock web server for binding site search and flexible docking, Methods 93 (2016) 72–83.
[39] M. Kurcinski, M. Pawel Ciemny, T. Oleniecki, A. Kuriata, A.E. Badaczewska-Dawid, A. Kolinski, S. Kmiecik, CABS-dock standalone: a toolbox for flexible protein-peptide docking, Bioinformatics 35 (20) (2019) 4170–4172.
[40] P. Teriete, S. Banerji, M. Noble, C.D. Blundell, A.J. Wright, A.R. Pickford, E. Lowe, D.J. Mahoney, M.I. Tammi, J.D. Kahmann, I.D. Campbell, A.J. Day, D.G. Jackson, Structure of the regulatory hyaluronan binding domain in the inflammatory leukocyte homing receptor CD44, Mol. Cell 13 (4) (2004) 483–496.
[41] G. Macindoe, L. Mavridis, V. Venkatraman, M.D. Devignes, D.W. Ritchie, HexServer: an FFT-based protein docking server powered by graphics processors, Nucleic Acids Res. 38 (2010) W445–W449.
[42] R. Thomas, J. Chen, M.M. Roudier, R.L. Vessella, L.E. Lantry, A.D. Nunn, In vitro binding evaluation of 177Lu-AMBA, a novel 177Lu-labeled GRP-R agonist for systemic radiotherapy in human tissues, Clin. Exp. Metastais 26 (2) (2009) 105–119.
[43] H.Y. Park, K.J. Lee, S.J. Lee, M.Y. Yoon, Screening of peptides bound to breast cancer stem cell specific surface marker CD44 by phage display, Mol. Biotechnol. 51 (3) (2012) 212–220.
[44] W. Li, H. Jia, J. Wang, H. Guan, Y. Li, D. Zhang, Y. Tang, T.D. Wang, S. Lu, A CD44-specific peptide, RP-1, exhibits capacities of assisting diagnosis and predicting prognosis of gastric cancer, Oncotarget 8 (18) (2017) 30063–30076.
[45] D. Zhang, J. Huang, W. Li, Z. Zhang, M. Zhu, Y. Feng, Y. Zhao, Y. Li, S. Lu, S. He, Screening and identification of a CD44v6 specific peptide using improved phage display for gastric cancer targeting, Ann. Transl. Med. 8 (21) (2020) 1442.
[46] Q. Li, K. Chen, W. Huang, H. Ma, X. Zhao, J. Zhang, Y. Zhang, C. Fang, L. Nie, Minimally invasive photothermal ablation assisted by laparoscopy as an effective preoperative neoadjuvant treatment for orthotopic hepatocellular carcinoma, Cancer Lett. 496 (2021) 169–178.
[47] Q. Yu, S. Huang, Z. Wu, J. Zheng, X. Chen, L. Nie, Label-free visualization of early cancer hepatic micrometastasis and intraoperative image-guided surgery by photoacoustic imaging, J. Nucl. Med. 61 (7) (2020) 1079–1085.
[48] S.Y. Lee, C.S. Ahn, Y.I. Yoon, S.G. Lee, S. Hwang, K.H. Kim, D.B. Moon, T.Y. Ha, G. W. Song, D.H. Jung, G.C. Park, Long-term outcomes of liver resection for multiple hepatocellular carcinomas: single-institution experience with 187 patients, Ann. Hepatobiliary Pancreat. Surg. 24 (4) (2020) 437–444.
[49] J. Lee, E.H. Cho, S.B. Kim, R. Kim, Prognosis after intrahepatic recurrence in the patients who underwent curative resection for hepatocellular carcinoma, Ann. Hepatobiliary Pancreat. Surg. 24 (4) (2020) 431–436.
[50] R.T. Poon, S.T. Fan, C.M. Lo, C.L. Liu, J. Wong, Long-term survival and pattern of recurrence after resection of small hepatocellular carcinoma in patients with preserved liver function: implications for a strategy of salvage transplantation, Ann. Surg. 235 (3) (2002) 373–382.
[51] T. Ishizawa, A. Saiura, N. Kokudo, Clinical application of indocyanine green-fluorescence imaging during hepatectomy, Hepatobiliary Surg. Nutr. 5 (4) (2016) 322–328.
[52] Y. Nakaseko, T. Ishizawa, A. Saiura, Fluorescence-guided surgery for liver tumors, J. Surg. Oncol. 118 (2) (2018) 324–331.
[53] A.D. Jones, J.C. Wilton, Can intra-operative fluorescence play a significant role in hepatobiliary surgery? Eur. J. Surg. Oncol. 43 (9) (2017) 1622–1627.
[54] J. Lv, Y. Xu, L. Xu, L. Nie, Quantitative functional evaluation of liver fibrosis in mice with dynamic contrast-enhanced photoacoustic imaging, Radiology 300 (1) (2021) 89–97.
[55] H. Maeda, J. Wu, T. Sawa, Y. Matsumura, K. Hori, Tumor vascular permeability and the EPR effect in macromolecular therapeutics: a review, J. Control Release 65 (1–2) (2000) 271–284.
[56] S. Caruso, J.C. Nault, A. Dive, Into the deep heterogeneity of hepatocellular carcinoma, Gastroenterology 157 (6) (2019) 1477–1479.

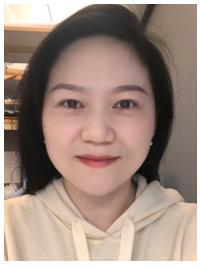

**Xiaoli Wu** received the Ph.D. degree in cell biology from University of Science and Technology of China. She works as a research fellow in the Department of Internal Medicine and Division of Gastroenterology at the University of Michigan. Her research focuses on identification and validation of specific imaging probes for early cancer detection.

**Xiaoqing Meng** is a postdoctoral research fellow in the Department of Internal Medicine and Division of Gastroenterology at the University of Michigan. Her research mainly focuses on the development of small-molecule non-invasive theranostic probe, near-infrared fluorescence I-II fluorescent imaging, photoacoustic imaging, and sub cellular organelles-targeting theranostics for cancer. Specifically, she designs cancer cell surface protein targeted peptide probes to track cancer cells in vivo to realize real-time monitoring of cancer. In addition, she aims to provide a promising tool for future clinical translation in treatment of patients with cancer, including accurate early cancer detection and image-guided surgery.

**Tse-Shao Chang** received the B.S. degree from National Cheng Kung University, Tainan, Taiwan, in 2014 and the M.S.E. degree from the University of Michigan, Ann Arbor, MI, USA, in 2018, both in mechanical engineering. He is currently a Ph.D. candidate in the Department of Mechanical Engineering at the University of Michigan, Ann Arbor, MI, USA. His research interests include biomedical optics, optical imaging, photoacoustic imaging, and mechatronics.

**Shuo Feng** is a postdoctoral research scientist in the Department of Medicine, Division of Gastroenterology, University of Michigan. Her research mainly focuses on design, development and validation of novel targeted peptides or nanoparticles for diagnosis and therapy of hepatocellular carcinoma. She performs imaging for early cancer detection and image-guided surgery using a variety of platforms, including optical imaging, ultrasound, MRI, photoacoustic imaging, and laparoscope.

**Miki Lee** received the B.S.E. degree in aerospace engineering and M.E. degree in space engineering from the University of Michigan, Ann Arbor, MI, USA, in 2015 and 2016, respectively. Since 2016, she has been a Research Lab Specialist with the Department of Internal Medicine, University of Michigan. Her research interest includes the development of endomicroscopy systems for molecular imaging applications.

**Sangeeta Jaiswal** is research lab specialist in the Prof. Wang lab at University of Michigan's internal medicine department. She focuses on identification of biomarkers for early detection of cancer and drug response. She is also interested in developing organoid transplant models for preclinical studies on biomarker development and drug discovery.

**Eun-Young K. Choi** is a Clinical Assistant Professor of Pathology at the University of Michigan. Her clinical and research interests are in hepatobiliary and gastrointestinal pathology.

**Lam Tran** is a doctoral student in the Department of Biostatistics at the University of Michigan School of Public Health. His research focuses on the development of computational methods for the efficient analysis of large-scale gene expression panels, specifically in the context of cancer and other chronic diseases. Specifically, he has designed an algorithmic process that facilitates the integration of biobank information to increase model-based predictive accuracy of survival outcomes in small local datasets. In addition, he has also created a new heuristic to greatly accelerate fitting the constrained lasso.

**Hui Jiang** is an Associate Professor in the Department of Biostatistics, a Core Member of the University of Michigan Rogel Cancer Center, an Affiliated Faculty Member of the University of Michigan Center for Computational Medicine Bioinformatics, and an Affiliated Faculty Member of the Center for Statistical Genetics. He has expertize in statistical genomics and Bioinformatics, with an emphasis on statistical methods and software tools for the analysis of large-scale genomics data generated from modern high-throughput technologies. He has published on a wide range of topics, and his works have been incorporated into software tools used by biologists and bioinformaticians.

**Thomas D. Wang** received his B.S. degree in Mathematics and Physics from Harvey Mudd College, Ph.D. degree in medical engineering and medical physics from MIT, and M.D. degree from Harvard Medical School. He is currently a Professor of Medicine, Biomedical Engineering, and Mechanical Engineering at the University of Michigan and the H. Marvin Pollard Collegiate Professor of Endoscopy Research. His research interests are in the field of biomedical optics, photoacoustics, and molecular imaging (https://sites.google.com/a/umich.edu/wang_lab). He has developed a number of methods for targeted detection of overexpressed cancer biomarkers for diagnosis and therapy.